catalysts

MDPI

Article

Engineering of a Hybrid g-C_3N_4/ZnO-W/Co_x Heterojunction Photocatalyst for the Removal of Methylene Blue Dye

Misbah Malik [1], Sobhy M. Ibrahim [2], Muhammad Altaf Nazir [1], Asif A. Tahir [3], Muhammad Khurram Tufail [4], Syed Shoaib Ahmad Shah [5], Aqsa Anum [1], Muhammad Ahmad Wattoo [6] and Aziz ur Rehman [1,*]

1 Institute of Chemistry, The Islamia University of Bahawalpur, Bahawalpur 63100, Pakistan
2 Department of Biochemistry, College of Science, King Saud University, P.O. Box 2455, Riyadh 11451, Saudi Arabia
3 Solar Energy Research Group, Environment and Sustainability Institute, Faculty of Environment Science and Economy, University of Exeter, Penryn Campus, Penryn TR10 9FE, UK; a.tahir@exeter.ac.uk
4 College of Materials Science and Engineering, Qingdao University, Qingdao 266071, China
5 Department of Chemistry, School of Natural Sciences, National University of Sciences and Technology, Islamabad 44000, Pakistan
6 Department of Chemistry, The Quaid i Azam University Islamabad, Islamabad 15320, Pakistan
* Correspondence: draziz@iub.edu.pk or azizypk@yahoo.com

Abstract: Robust hybrid g-C_3N_4/ZnO-W/Co_x heterojunction composites were synthesized using graphitic carbon nitride (g-C_3N_4) and ZnO-W nanoparticles (NPs) and different concentrations of Co dopant. The hybrid heterojunction composites were prepared by simple and low-cost coprecipitation methods. The fabricated catalyst was explored and investigated using various characterization techniques such as FTIR, XRD, FESEM and EDX. The surface morphology of the as-prepared hybrid nanocomposites with particle sizes in the range of 15–16 nm was validated by SEM analysis. The elemental composition of the synthesized composites was confirmed by EDS analysis. Photocatalysis using a photon as the sole energy source is considered a challenging approach for organic transformations under ambient conditions. The photocatalytic activity of the heterojunctions was tested by photodegrading methylene blue (MB) dye in the presence of sunlight. The reduced band gap of the heterojunction composite of 3.22–2.28 eV revealed that the incorporation of metal ions played an imperative role in modulating the light absorption range for photocatalytic applications. The as-synthesized g-C_3N_4/ZnO-W/$Co_{0.010}$ composite suppressed the charge recombination ability during the photocatalytic degradation of methylene blue (MB) dye. The ternary heterojunction C_3N_4/ZnO-W/$Co_{0.010}$ composite showed an impressive photocatalytic performance with 90% degradation of MB under visible light within 90 min of irradiation, compared to the outcomes achieved with the other compositions. Lastly, the synthesized composites showed good recyclability and mechanical stability over five cycles, confirming them as promising photocatalyst options in the future.

Keywords: doping; hybrid heterojunction; g-C_3N_4/ZnO-W/Co_x; coprecipitation; photocatalytic degradation; methylene blue

Citation: Malik, M.; Ibrahim, S.M.; Nazir, M.A.; Tahir, A.A.; Tufail, M.K.; Shah, S.S.A.; Anum, A.; Wattoo, M.A.; Rehman, A.u. Engineering of a Hybrid g-C_3N_4/ZnO-W/Co_x Heterojunction Photocatalyst for the Removal of Methylene Blue Dye. *Catalysts* **2023**, *13*, 813. https://doi.org/10.3390/catal13050813

Academic Editor: Enshirah Da'na

Received: 28 March 2023
Revised: 13 April 2023
Accepted: 25 April 2023
Published: 27 April 2023

1. Introduction

Extensive adulteration owing to global industrialization, commercialization and agricultural practices causes the excessive release of organic pollutants. Water pollution has become one of the most serious environmental issues due to the massive pollution of freshwater reservoirs. Wastewater discharged from industry and numerous human activities has triggered death-defying environmental impacts [1]. A frightening percentage of individuals suffering everyday unavailability of clean drinking water and this unsophisticated negligence from several industrial units for releasing wastewater without any handling into freshwater streams has posed grave threats to human health. Priorly, conventional

remediation techniques such as activated carbon adsorption, filtration, extraction, oxidation, ultrafiltration, electrolysis, chemical oxidation and biological treatment were applied, and usually, the results of incomplete mineralization of pollutants were obtained. The present progressive research in the field of various advanced oxidation technologies has overcome the inadequacies of these conventional techniques [2]. A lot of researchers have made phenomenal exertions to explore more catalysts and innovative materials to degrade toxic organic pollutants of wastewater and have, providentially, found semiconductor photocatalysis technology as a significant treatment to partially solve energy shortages and water pollution problems [3,4]. Among the diverse, sustainable developments of recent years, ultraviolet (UV) and visible light active photocatalyst comprised various semiconductors such as TiO_2, ZnS, Fe_2O_3, CdS, Bi_2WO_6, $InVO_4$, Ta_3N_5 and TaON [5] are the best approaches for aquatic decontamination.

While probing for active and visible light dynamic semiconductor photocatalysts, graphitic carbon nitride (g-C_3N_4) possesses an enthusiastic impression as a next-generation photocatalyst [6–11]. The temperature-controlled single-step polymerization of a low-cost and readily available nitrogen-rich precursor leads to the formation of a semiconductor catalyst [12–15]. g-C_3N_4 is a metal-free catalyst with the lowest energy band gap (Eg = 2.7–2.8 eV) among its seven polymeric phases because of sp^2-hybridised C and N having π-conjugated electronic systems. This substantially small band gap compared to TiO_2 is primarily responsible for absorption in the visible spectrum region [16]. Besides all of these advantages, regrettably, pristine g-C_3N_4 possesses some limitations which hamper the wide-scale usage of g-C_3N_4 such as sluggish efficacy of solar light utilization and high electron–hole pair's recombination, which leads to photoexcitation (in picoseconds). Moreover, the non-magnetic nature of carbon nitride has also hindered its practical implementation on industrial scale as it is quite hard to extract non-magnetic catalysts from enormous volumes of treated solutions [17,18]. The above-mentioned drawbacks associated with pristine g-C_3N_4 can be best addressed by adopting strategies including metal and non-metal doping and coupling carbon nitride with a variety of semiconductor metal oxides (SMO) [19–22]. Recently, numerous g-C_3N_4-based semiconductor nanocomposites such as $CuFe_2O_4$/g-C_3N_4 [23], g-C_3N_4/CeO_2 [24], WO_3/g-C_3N_4 [25], SnS_2/g-C_3N_4 [26] and $NiTiO_3$/g-C_3N_4 [27] have been reported for photocatalytic applications. These binary nanostructures exhibit meaningful enhanced photocatalytic activity compared to pristine nanostructures. This could be attributed to the improved generation of charge carriers, the suppression of the recombination of e^-/h^+ pairs, and the amended visible light utilization, leading to improved photocatalytic activity. Table 3 Comprised of the MB dye degradation results with the published literature.

Photocatalysis using a photon as the sole energy source is considered a challenging approach for organic transformations under ambient conditions [28]. Photocatalytic degradation is considered a clean and green purification procedure in wastewater treatment chiefly because of its non-toxic end products, and metal oxide semiconductor photocatalysts play a vital role in the degradation of water pollutants [25,29,30]. Among the different metal oxide semiconductor photocatalytic materials, ZnO and TiO_2 are widely applicable for environmental applications because they exhibit high chemical stability and strong oxidizing power and are highly economical [31,32]. B. Dindar et al. investigated ZnO as a promising photoactive material for the degradation of phenol [33,34]. Gouvea et al. found ZnO to be a more effective material for the degradation of organic matter in an aqueous solution [35]. Laziouti et al. studied the band gap, which revealed that ZnO has a high degrading efficiency due to its increased light conversion efficacy [36]. Previous research has shown ZnO to be the most promising photocatalytic material, but its large band gap of 3.37 eV only allows for 3–5% absorption of solar light in the visible region, and fast electron–hole pair recombination has hampered its practical application [37]. Many efforts have been made to overcome the inadequacies associated with ZnO by stretching its adsorption range to the visible light region via doping or coupling with metals, non-metals and carbon-based materials or in heterojunction with some visible band gap

semiconductor materials [38,39]. Heterojunction with transition metals is quite beneficial because of their 4f and 5d electronic configuration, which fascinate the charge carriers and delay the recombination of the electron–hole pair resulting in improved degradation efficacy. As reported earlier, among the transition metals, a tungsten (W) heterojunction with ZnO remarkably enhances the photocatalytic activity for maximum use of the solar spectrum. The distinguishing half-filled valance shell and oxidation state corresponding to tungsten metal generate intermediate energy levels between the standard energy level of ZnO, resulting in the enhancement of charge carriers in the ZnO system [40]. It is worth mentioning here that the ionic radii of W^{+6} (0.64 nm) are relatively smaller than that of Zn^{2+} (0.74 nm); because of this, W^{+6} can effortlessly substitute Zn^{2+} ions in the ZnO lattice. As we can see, the Zn^{2+} and W^{+6} atoms have an electronic difference of four, and each tungsten atom has the ability to donate one or more electrons to the lattice, increasing the photocatalytic activity [41].

The current work aimed to improve the photocatalytic competence of nanocomposites by creating a hybrid heterojunction of g-C_3N_4, ZnO-W and the addition of cobalt metal in various concentrations of g-C_3N_4/ZnO-W/Co_x. The consequence of transition metal doping on the optical properties of g-C_3N_4 and ZnO has been explored. Transition-metal-doped g-C_3N_4/ZnO-W/Co_x composites have been investigated using various characterization techniques such as XRD, FTIR and SEM. The designed heterostructure exhibits a structure that may hinder the recombination rate of photoinduced electron–hole (e^-/h^+) pairs and act as mighty adsorbents for the pollutant molecules. The resulting hybrid exhibited outstanding photocatalytic and cycling stability under visible light irradiation. The photoactivity of the as-synthesized g-C_3N_4/ZnO-W/Co_x hybrid heterojunction nanocomposite towards methylene blue (MB) dye solution was evaluated separately for each sample. MB was selected as a model pollutant due to its wide usability in many industries such as the textile, dyeing, printing, paper and plastic industries. It causes mutagenic and carcinogenic effects in living organisms [42,43]. The concentration of Co dopant was varied and its effect on the photocatalytic ability of the synthesized catalyst was systematically investigated. This study proposes an active method that addresses environmental pollutants using hybrid heterojunction nanocomposite-based catalysts for wastewater treatment.

2. Results and Discussion

2.1. XRD Analysis

The effect of Co doping and W modification in the crystal phases of the synthesized hybrid heterojunction nanocomposite g-C_3N_4/ZnO-W/Co_x were characterized by the X-ray diffraction (XRD) technique. The XRD pattern of the synthesized hybrid nanocomposite is shown in Figure 1a–f, which indicates that sharp and strong diffraction peaks in the spectral images of synthesized photocatalyst are well matched with ZnO (hexagonal wurtzite, space group: P63mc) and g-C_3N_4 (hexagonal, space group: P-6m2). There is no additional peak belonging to secondary phases or hydroxides observed in all samples. The intense and sharp diffraction spectral pattern corresponds to the highly crystalline nature of the grown nanocomposites. The XRD spectra of the grown nanocomposites with varied cobalt concentrations showed diffraction peaks of ZnO (JCPDS card No. 00-001-1136) at 2θ = 31.8°, 34.3°, 36.4°, 47.5°, 57.1°, 63.2°, 67.8°, 68.9° and 76.8° with the corresponding Miller indices of (100), (002), (101), (102), (110), (103), (112), (201) and (202) and peaks of g-C_3N_4 (JCPDS card No. 01-087-1526) at 2θ = 13.1°, 21.6°, 25.3°, 26.5°, 37.9°, 40.3°, 44.0°, 52.1°, 59.3°, 59.5°, 70.0° and 74.1° with the corresponding Miller indices of (001), (100), (101), (002), (110), (003), (200), (202), (104), (210), (301) and (105), respectively. A weak peak observed at 2θ = 13.40° exhibiting Miller indices values of (001) corresponds to a tri-s-triazine unit of carbon nitride. The decrease in the intensity of this peak in some samples may be attributed to more random plane ordering during the condensation reaction to form the g-C_3N_4 structure. The peak may be reduced with the increasing dopant concentration, indicating strong interaction between the host and dopant species [44,45]. The strong peak at 26.5° is attributed to the long-range interlayer stacking reflection of the

conjugated aromatic system and corresponds to graphitic materials. [46]. The diffraction peak of g-C_3N_4 remains integral, confirming that metal doping does not affect the peaks of carbon nitride, but a decreased peak intensity in the composites corresponds to the effective insertion of the dopant [47]. All of the characteristic peaks of carbon nitride and ZnO are present in the hybrid composite but with lesser intensities suggesting successful synthesis of the crystalline nature composites. The crystallite size of the synthesized composites was determined by the Scherrer equation.

$$D = (k\lambda/\beta hkl\ \cos\theta), \quad (1)$$

where D is the particle size (nm), λ is the wavelength of the radiation (Å), k is the constant coefficient (0.94), βhkl is the peak width at half-maximum intensity and θ is the peak position [48]. In the present research and according to this equation, the crystallite size of all samples was about 15–16 nm. Different structural parameters of g-C_3N_4/ZnO-W/Co_x nanocomposites determined from spectral XRD patterns are shown in Table 1.

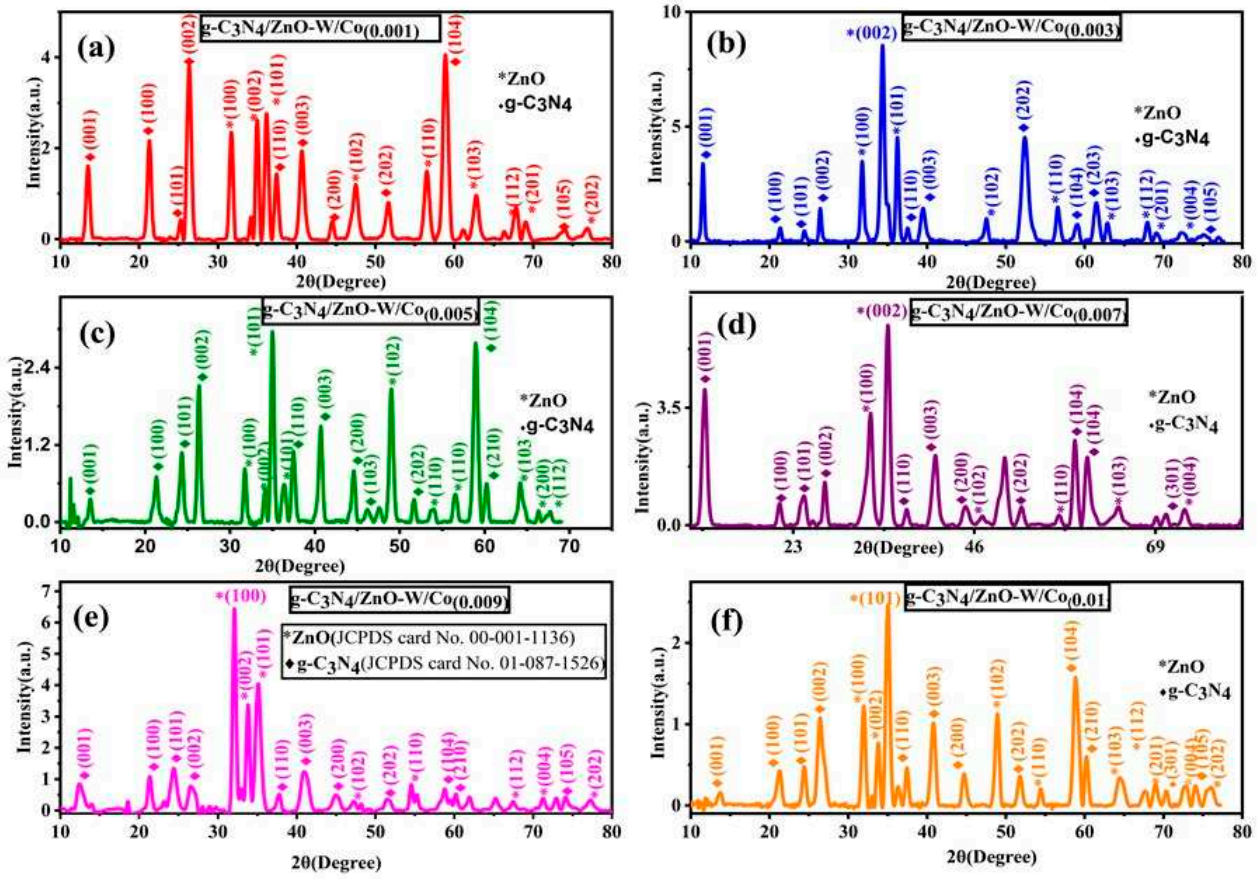

Figure 1. XRD patterns of the g-C_3N_4/ZnO-W/Co_x hybrid heterojunction nanocomposites: (**a**) g-C_3N_4/ZnO-W/$Co_{(0.001)}$, (**b**) g-C_3N_4/ZnO-W/$Co_{(0.003)}$, (**c**) g-C_3N_4/ZnO-W/$Co_{(0.005)}$, (**d**) g-C_3N_4/ZnO-W/$Co_{(0.007)}$, (**e**) g-C_3N_4/ZnO-W/$Co_{(0.009)}$ and (**f**) g-C_3N_4/ZnO-W/$Co_{(0.01)}$.

Table 1. Geometric parameters of g-C_3N_4/ZnO-W/Co_x nanocomposites determined by XRD analysis.

Sample	a (Å)	c (Å)	Volume (Å)^3	Crystallite Size (nm)	Strain ε (nm^{-2})	Dislocation Density	Lattice Spacing
g-C_3N_4/ZnO-W/$Co_{(0.001)}$	3.432	6.029	61.523	15.183	2.424×10^{-6}	4.337×10^{-6}	2.731
g-C_3N_4/ZnO-W/$Co_{(0.003)}$	3.265	5.748	53.092	15.811	2.353×10^{-6}	3.999×10^{-6}	2.742
g-C_3N_4/ZnO-W/$Co_{(0.005)}$	3.392	5.964	59.454	15.823	2.351×10^{-6}	3.994×10^{-6}	2.715
g-C_3N_4/ZnO-W/$Co_{(0.007)}$	3.306	5.820	55.113	15.840	2.349×10^{-6}	3.985×10^{-6}	2.794
g-C_3N_4/ZnO-W/$Co_{(0.009)}$	3.312	5.829	55.412	15.786	2.356×10^{-6}	4.012×10^{-6}	2.793
g-C_3N_4/ZnO-W/$Co_{(0.010)}$	3.231	5.689	51.440	15.826	2.351×10^{-6}	3.992×10^{-6}	2.721

2.2. FTIR Analysis

The FTIR spectra of various metal-doped hybrid composites are shown in Figure 2a–f. The FTIR spectra were recorded in the range of 500 cm^{-1} to 4500 cm^{-1} for the elucidation of various functional groups existing in the synthesized hybrid nanocomposite. The FTIR analysis revealed all the characteristic transmittance peaks of g-C_3N_4, ZnO and W, confirming the synthesis of the hybrid composites. The formation of the ZnO wurtzite structure and the effect of W addition in ZnO were characterized by FT-IR spectral analysis, as shown in Figure 2a–f. The peaks in the vicinity of 600–700 cm^{-1} are attributed to the formation of a metal–oxygen bond and belong to the vibrational bending mode of Zn–O, whereas the absorption peak above 1000 cm^{-1} corresponds to the stretching mode of the Zn–O bond [49]. The two peaks in the region of 630–780 cm^{-1} correspond to the O-W-O and W-O-W groups. An absorption peak at 800–850 cm^{-1} corresponds to the 1,3,5-triazine ring breathing model [50]. The peak in the region of 1200–1600 cm^{-1} corresponds to the stretching vibrations of CN heterocycles. The absorption band observed at 1630–1640 cm^{-1} was due to stretching vibrations of C=C [51]. The broad band at 3100 cm^{-1} belongs to the vibrational mode of the residual N–H group of graphitic carbon nitride, whereas the broad band at 3500 cm^{-1} and in the range of 1600 cm^{-1} is attributed to the stretching of water and hydroxyl groups on the surface of the sample molecules [52,53]. An absorption peak observed at 2300–2400 cm^{-1} was attributed to metal doping in ZnO [54]. A small absorption peak at 2000 to 2100 cm^{-1} accounts for the additional stretching modes observed due to the interaction of the metal with g-C_3N_4 and ZnO. The absorption band located at 950–1000 cm^{-1} corresponds to the symmetric stretching of W=O bond cluster boundaries [55].

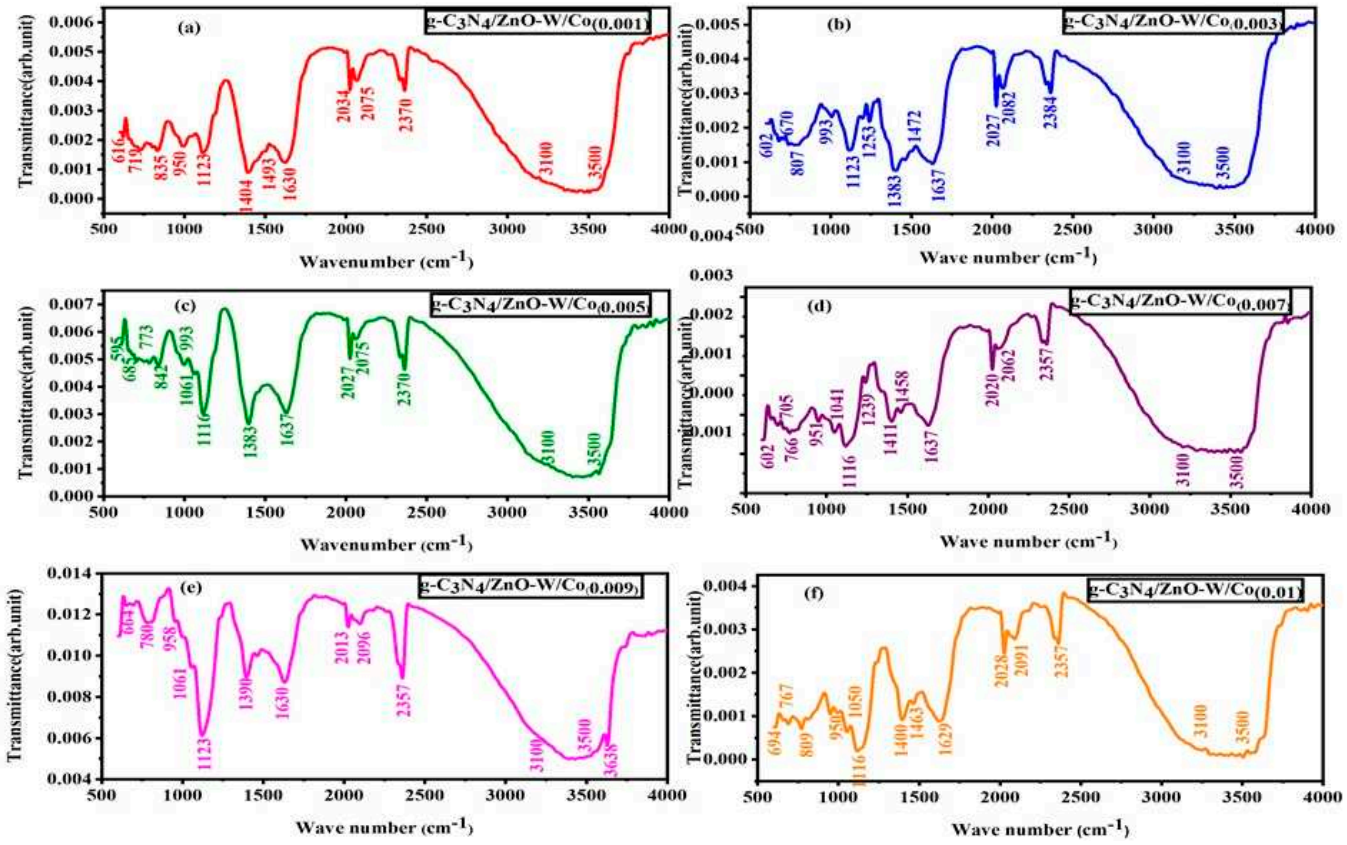

Figure 2. FTIR spectra of the g-C_3N_4/ZnO-W/Co_x hybrid heterojunction nanocomposites: (**a**) g-C_3N_4/ZnO-W/$Co_{(0.001)}$, (**b**) g-C_3N_4/ZnO-W/$Co_{(0.003)}$, (**c**) g-C_3N_4/ZnO-W/$Co_{(0.005)}$, (**d**) g-C_3N_4/ZnO-W/$Co_{(0.007)}$, (**e**) g-C_3N_4/ZnO-W/$Co_{(0.009)}$ and (**f**) g-C_3N_4/ZnO-W/$Co_{(0.01)}$.

2.3. SEM and EDS Analysis

The geometrical shape, morphology and porosity of the synthesized composites are the main factors to determine the degradation efficiency of the photocatalyst and were well evaluated by scanning electron microscopy (SEM). The representative field emission scanning electron microscopy (FESEM) images in the presence of Co dopant are illustrated in Figure 3a–f and show the morphology of the synthesized hybrid composites, revealing a uniform and smooth sheet-like structure with aggregation of particles as an outcome of metal doping on carbon nitride. Firstly, the deposition of W did not affect the rod-like structure, average lengths and diameters of the ZnO nanorods, as shown in Figure 3a–f [56]. It can be seen that the ZnO-W dispersed irregularly in the form of small particles on the surface of g-C_3N_4. The heterojunction of ZnO-W and g-C_3N_4 causes no drastic effect on the morphology of ZnO-W [57]. The metal-doped material exhibited a thick micro-size morphology distributed unevenly over the area of the sample. The interface of ZnO with g-C_3N_4 grew into a slacked interlinked network consisting of elongated fibers and led to the formation of a structure with an increased surface area, which may result from gases that evolved during the thermal polymerization reaction. The SEM study revealed a particle size of 15–16 nm. No prominent difference in the morphology, particle size and shape of the samples with different concentrations of doped metals was observed [58].

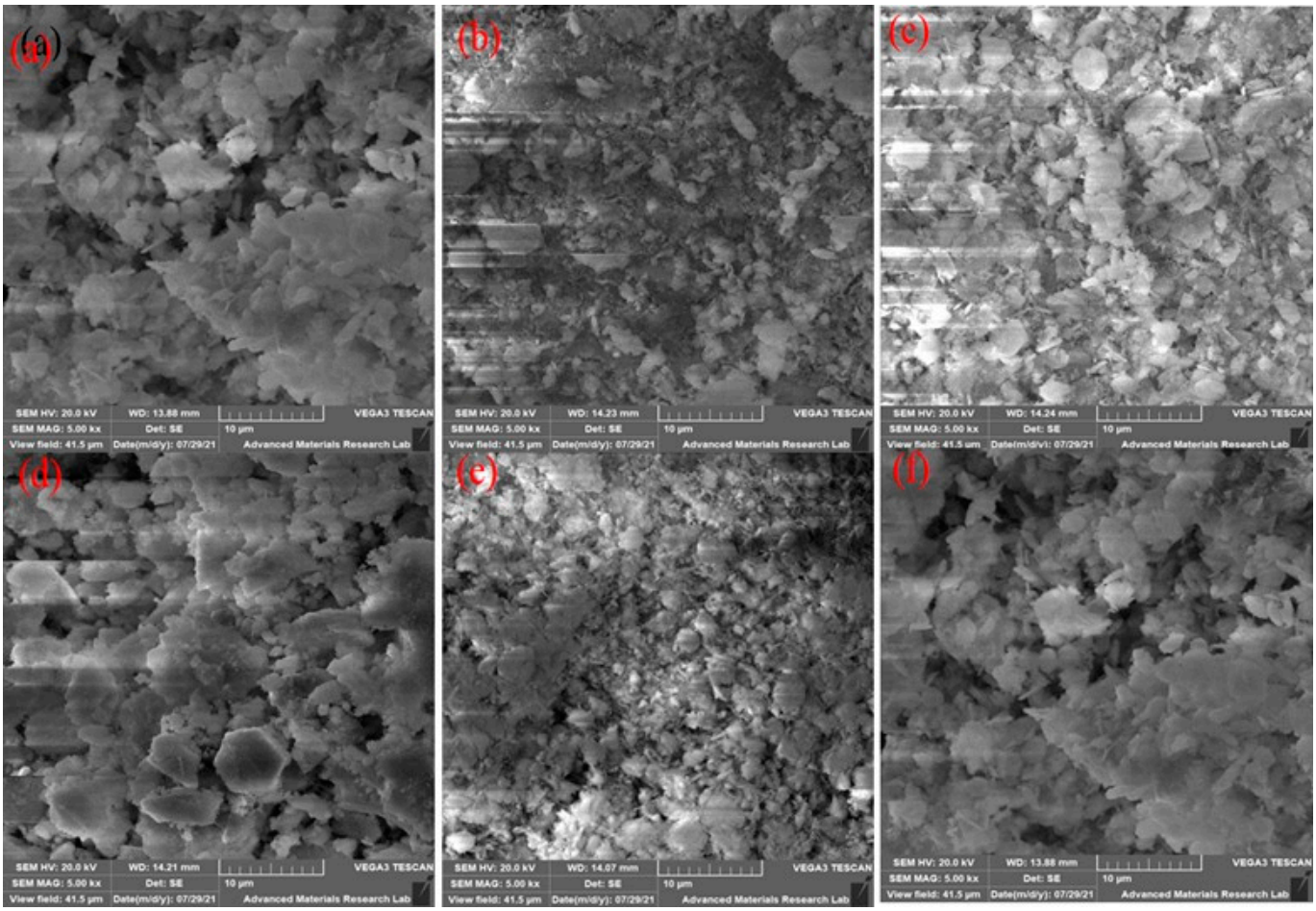

Figure 3. SEM micrographs of the g-C_3N_4/ZnO-W/Co_x hybrid heterojunction nanocomposites: (**a**) g-C_3N_4/ZnO-W/$Co_{(0.001)}$, (**b**) g-C_3N_4/ZnO-W/$Co_{(0.003)}$, (**c**) g-C_3N_4/ZnO-W/$Co_{(0.005)}$, (**d**) g-C_3N_4/ZnO-W/$Co_{(0.007)}$, (**e**) g-C_3N_4/ZnO-W/$Co_{(0.009)}$ and (**f**) g-C_3N_4/ZnO-W/$Co_{(0.01)}$.

Energy-dispersive X-ray (EDX) is a widely employed tool used by today's materials scientists and is used in conjunction with SEM (scanning electron microscopy). An EDX

detector delivers more supplementary evidence about a sample than SEM alone. EDX spectral analysis generates quick qualitative information as well as a sample. The typical EDS spectrum of g-C_3N_4/ZnO-W/Co_x is shown in Figure 4 and confirms the formation of a carbon nitride–ZnO-W heterojunction with cobalt metal. Peaks attributed to C, N, O, Zn, W and Co reveal quantitative information, enabling researchers to identify both types of elements as well as the percentage of each element's concentration within the elemental composition of the synthesized hybrid nanocomposites. The reactants used were chlorides and sulphates; hence, the unsolicited peaks attributed to Cl, S and Mn were also experiential, thus corresponding to impurities present within the sample. The high-weight oxygen peak in the spectrum was also observed and belonged to environmental oxygen in the scanned sample [55].

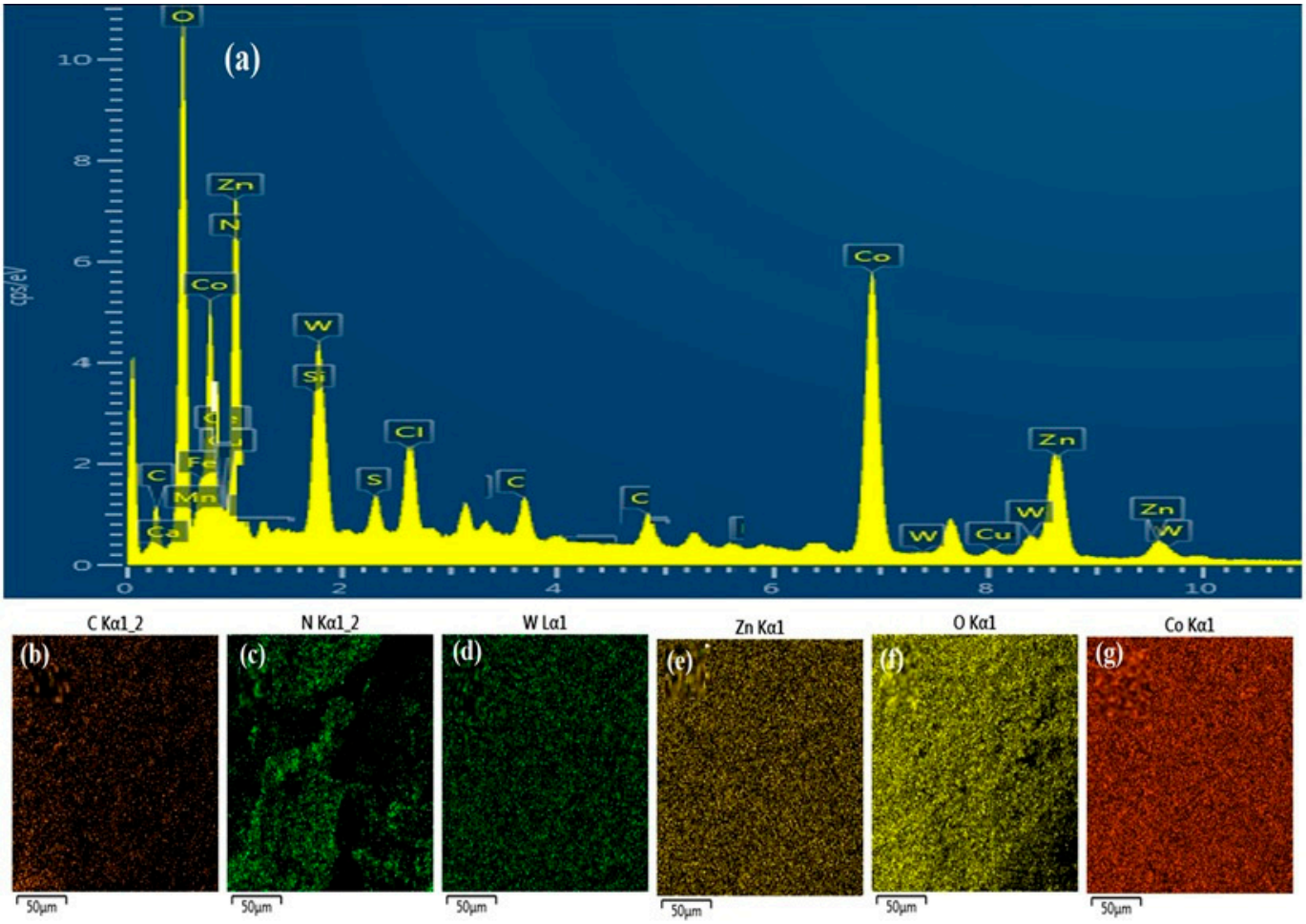

Figure 4. (**a**) EDS spectrum of the g-C_3N_4/ZnO-W/$Co_{(0.01)}$ hybrid heterojunction composite. (**b**–**g**) elemental mapping images of C, N, W, Zn, O and Corespectively.

2.4. Optical Analysis/Band Gap Tuning

To understand the optical properties of the prepared nanocomposites, a valuation of optical response was carried out by recording UV visible spectra and then defining the band gap energies of the synthesized hybrid nanocomposites in the range of 200–800 nm. The absorbance spectra and band gap energies of the synthesized nanocomposites with varying cobalt concentrations are shown in Figures 5a–f and 6a–f, respectively. The established heterojunction between carbon nitride ZnO-W and dopant metal cobalt enhanced the light absorption ability of the synthesized composites. g-C_3N_4/ZnO-W/$Co_{(0.10)}$ exhibited more absorption in the visible region as compared to other cobalt concentrations and possessed the highest photocatalytic activity [41]. It was observed that an increase in the

concentration of dopant metal causes increases in light absorption intensity and the number of photogenerated (e^-/h^+) pairs and thus, the enrichment observed in the number of active species, which enhances the photocatalytic activity of the sample [59].

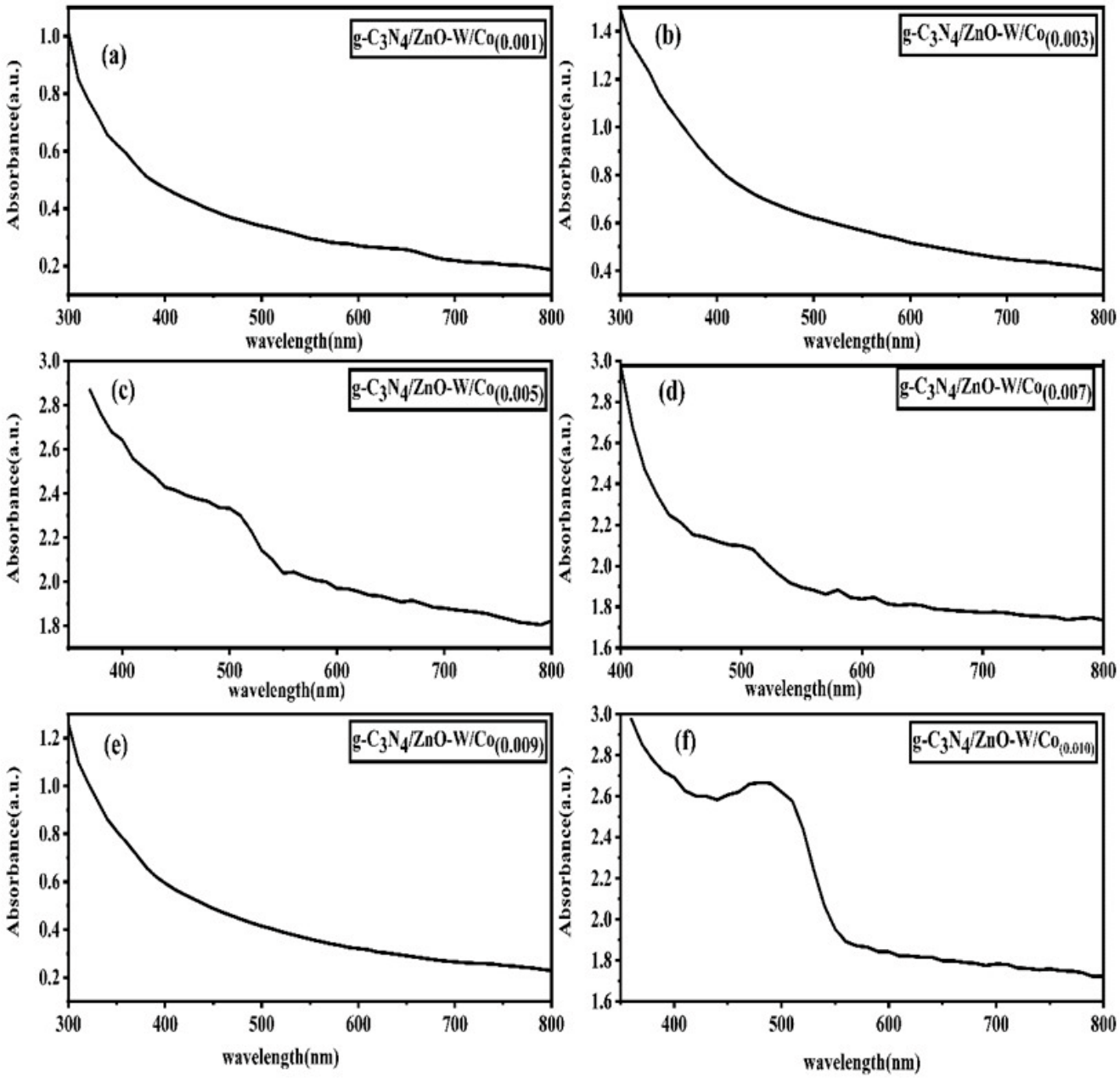

Figure 5. Absorbance spectra of the g-C_3N_4/ZnO-W/Co_x hybrid heterojunction composites: (**a**) g-C_3N_4/ZnO-W/$Co_{(0.001)}$, (**b**) g-C_3N_4/ZnO-W/$Co_{(0.003)}$, (**c**) g-C_3N_4/ZnO-W/$Co_{(0.005)}$, (**d**) g-C_3N_4/ZnO-W/$Co_{(0.007)}$, (**e**) g-C_3N_4/ZnO-W/$Co_{(0.009)}$ and (**f**) g-C_3N_4/ZnO-W/$Co_{(0.01)}$.

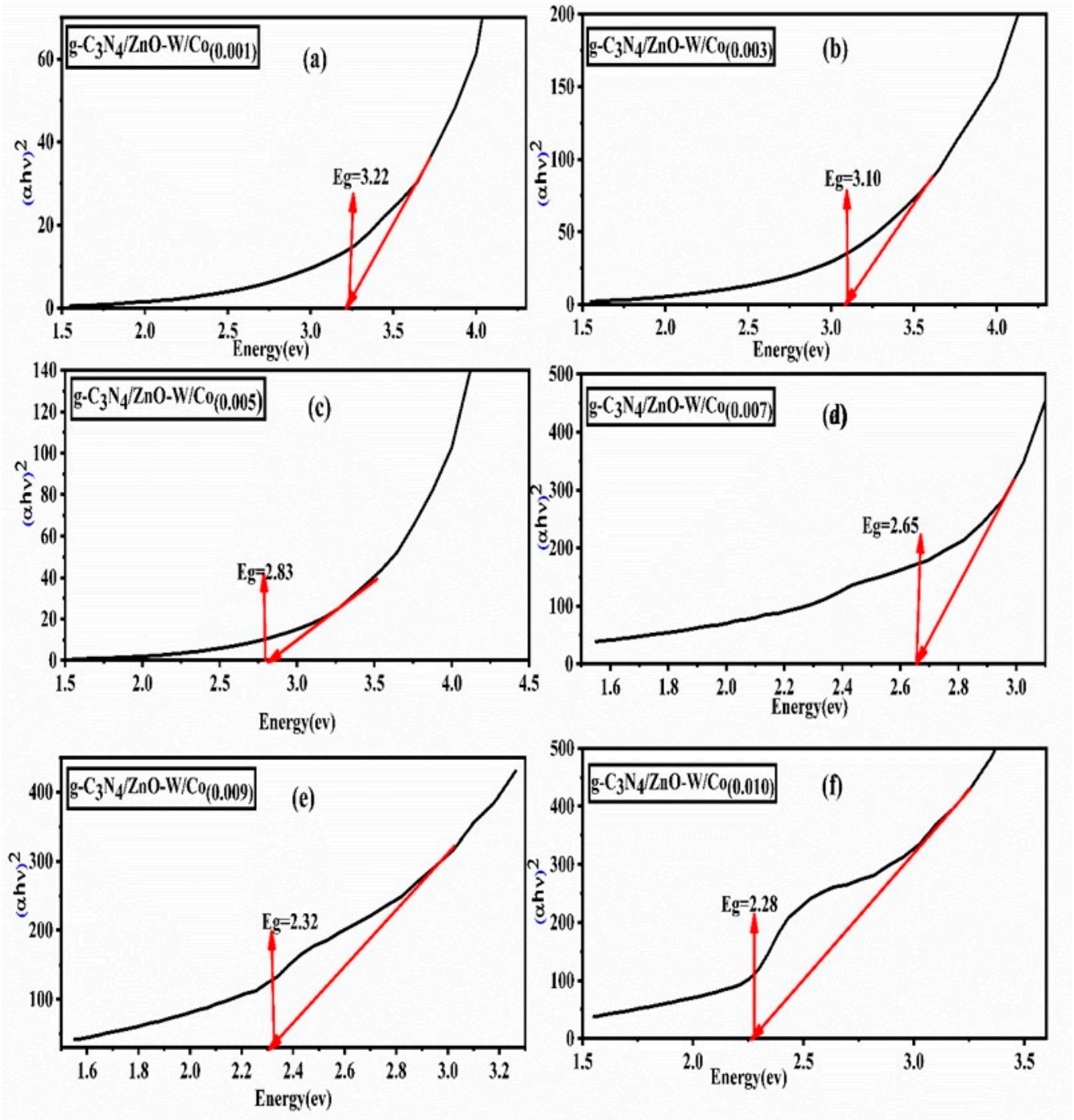

Figure 6. The Tauc plots of the g-C_3N_4/ZnO-W/Co_x hybrid heterojunction nanocomposites with different doping (cobalt) concentrations: (**a**) g-C_3N_4/ZnO-W/$Co_{(0.001)}$, (**b**) g-C_3N_4/ZnO-W/$Co_{(0.003)}$, (**c**) g-C_3N_4/ZnO-W/$Co_{(0.005)}$, (**d**) g-C_3N_4/ZnO-W/$Co_{(0.007)}$, (**e**) g-C_3N_4/ZnO-W/$Co_{(0.009)}$ and (**f**) g-C_3N_4/ZnO-W/$Co_{(0.01)}$.

Using the Tauc plots of the band gap energies of the g-C_3N_4/ZnO-W/Co_x hybrid heterojunction nanocomposites (x = 0.001, 0.003, 0.005, 0.007, 0.009 and 0.01 M), they followed the order of 3.22, 3.10, 2.83, 2.65, 2.32 and 2.28 eV, respectively. These values indicate that a significant decrease in the band gap values of the synthesized hybrid heterojunction composites is observed with an increase in the concentration of cobalt (doped metal) [60]. The hybridization of ZnO-W with g-C_3N_4 and cobalt triggered a decrease in the band gap energy, and this reduced band gap of g-C_3N_4/ZnO-W/Co could lead to

better absorption of light in the visible region preferring more electron–hole (e^-/h^+) pair formation and thus resulting in heightened photocatalytic activity. Among the synthesized nanocomposites of varying cobalt concentrations, g-C_3N_4/ZnO-W/$Co_{(0.010)}$ exhibited the lowest band gap value of 2.28 eV, enabling the hybrid heterojunction nanocomposite to degrade the pollutant more efficiently [61].

2.5. Photocatalytic Activity

The photocatalytic activity of the g-C_3N_4/ZnO-W composites was analyzed as a function of Co_x doping concentration (x = 0.001, 0.003, 0.005, 0.007, 0.009 and 0.010). It is imperative to mention here that all the synthesized composites were found to be photo-catalytically active. The spectral images representing the photocatalytic degradation of the examined dye are shown in Figure 7a–f. The degradation efficiency of g-C_3N_4/ZnO-W/Co_x follows the order g-C_3N_4/ZnO-W/$Co_{(0.010)}$ > g-C_3N_4/ZnO-W/$Co_{(0.009)}$ > g-C_3N_4/ZnO-W/$Co_{(0.007)}$ > g-C_3N_4/ZnO-W/$Co_{(0.005)}$ > g-C_3N_4/ZnO-W/$Co_{(0.003)}$ > g-C_3N_4/ZnO-W/$Co_{(0.001)}$ with 90 %, 87 %, 85 %, 82 %, 78 % and 75 %, respectively, under the irradiation time of 90 min. It is observed that the degradation efficiency of g-C_3N_4/ZnO-W/$Co_{(0.010)}$ is higher as compared to other composites, thus revealing that an increased concentration of dopant metal increases the surface barrier resulting in a narrower charge region [55]. Consequently, this suppresses the electron–hole pair recombination and the enhancement in degradation activity. The concentration of doped metal plays an important role in the photodegradation mechanism of the as-synthesized catalyst. An optimum increase in the metal concentration provides amended results, but beyond this optimum amount, the excess metal particles cause agglomeration leading to the recombination of electron–hole pairs; thus, this could suppress the transfer rate of photo-induced charges and decrease the photocatalytic activity of the catalyst [45]. The linear fit model was applied to study the kinetics of the photodegradation reaction quantitatively, given as

$$C_t = C_0\, e^{-kt} \tag{2}$$

$$-\ln(C_t/C_0) = kt \tag{3}$$

where k is the first order rate constant. By plotting $-\ln(C_t/C_0)$ on the *y*-axis and irradiation time (t) on the *x*-axis, a straight line is obtained, as shown in Figure 9a and k is calculated from the slope. The calculated values of constant rate k for different dyes are shown in Table 2, whereas the R^2 values signify that the reaction exhibits first-order kinetics.

2.6. Photodegradation Mechanism

Theoretical deliberation of any semiconductor photocatalytic mechanism is based on the knowledge of conduction and valence band potentials and redox potentials. In order to accomplish photocatalytic reactions efficiently, the conduction band potentials must be more negative than the potentials of reduction reactions, while the valence band potentials must be located more positively than the potentials of oxidation reactions [62]. In general, irradiation of light on a photocatalytic material results in photogenerated an electron–hole pair. These electrons and holes combine with oxygen and water molecules resulting in the formation of strong hydroxyl radicals and super oxides, which cause the degradation of toxic organic dyes into non-toxic end products, e.g., H_2O, CO_2 and some mineral acids [63]. The pristine ZnO exhibits less activity than the W-doped material because the W-ion generates an intermediate energy level between the valance band and conduction band, causing the deception of photo-excited electrons from the conduction band level. This deception of electrons in the intermediate level deferred the recombination of the electron–hole pair resulting in enhanced photocatalytic activity. Another advantage associated with tungsten as a dopant is its ionic state, i.e., W^{+6}. When Zn^{+2} is replaced by a W^{+6} number of charge carriers in the ZnO system of semiconductor material increased and an improved degradation efficacy can be attained [64].

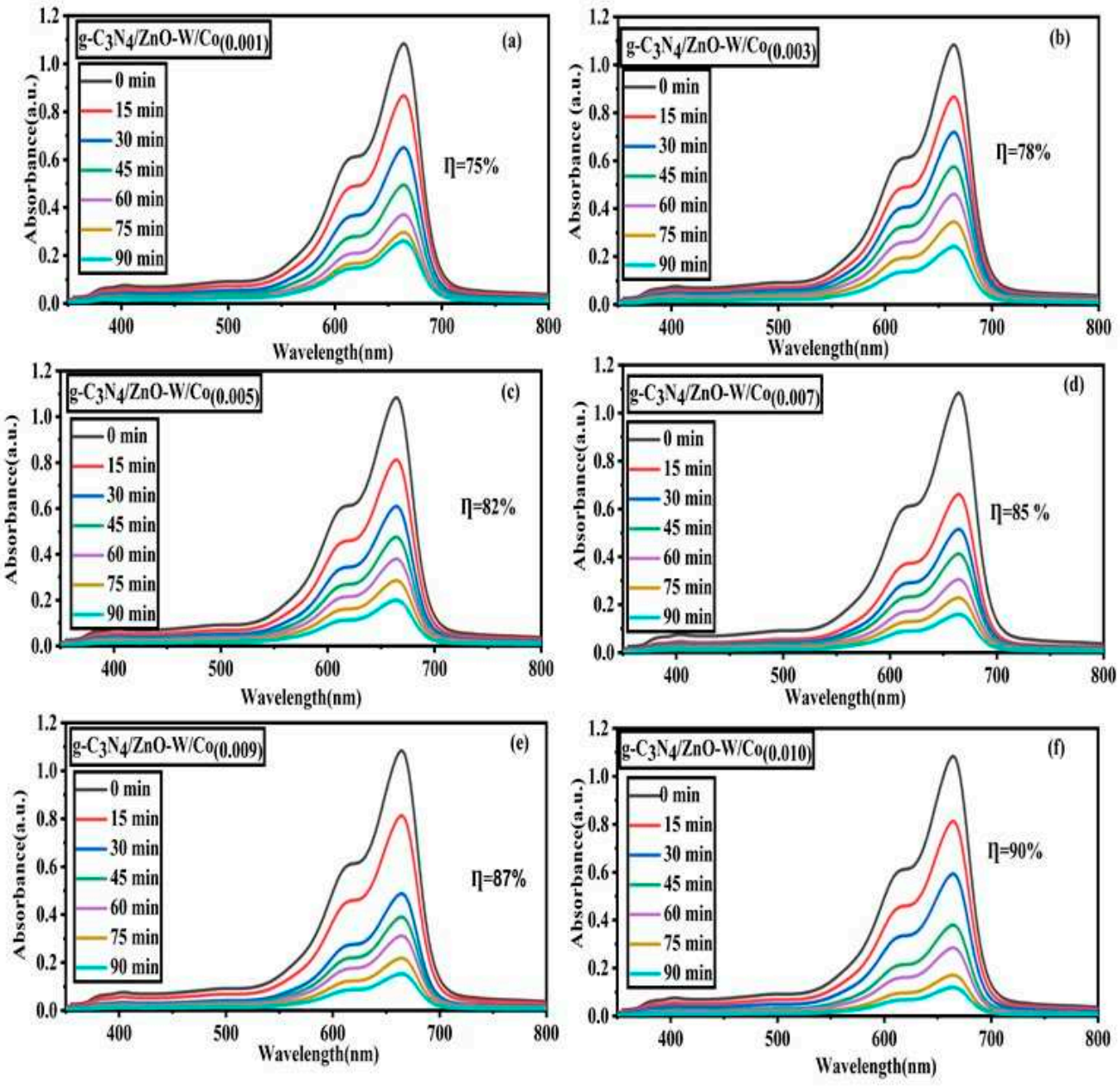

Figure 7. Photocatalytic degradation of the different g- C_3N_4/ZnO-W/Co_x hybrid heterojunction composites: (**a**) g-C_3N_4/ZnO-W/$Co_{(0.001)}$, (**b**) g-C_3N_4/ZnO-W/$Co_{(0.003)}$, (**c**) g-C_3N_4/ZnO-W/$Co_{(0.005)}$, (**d**) g-C_3N_4/ZnO-W/$Co_{(0.007)}$, (**e**) g-C_3N_4/ZnO-W/$Co_{(0.009)}$ and (**f**) g-C_3N_4/ZnO-W/$Co_{(0.01)}$.

Table 2. Degradation efficiency (%), kinetic rate constant (k) and R^2 values of the hybrid heterojunction nanocomposites.

Sample	Dye	Degradation Efficiency %	Rate Constant (k) (min^{-1})	R^2	Band Gap (±0.1 eV)
g-C_3N_4/ZnO-W/$Co_{(0.001)}$	MB	75	0.024	0.989	3.22
g-C_3N_4/ZnO-W/$Co_{(0.003)}$	MB	78	0.025	0.985	3.10
g-C_3N_4/ZnO-W/$Co_{(0.005)}$	MB	82	0.027	0.996	2.83
g-C_3N_4/ZnO-W/$Co_{(0.007)}$	MB	85	0.029	0.988	2.65
g-C_3N_4/ZnO-W/$Co_{(0.009)}$	MB	87	0.031	0.988	2.32
g-C_3N_4/ZnO-W/$Co_{(0.010)}$	MB	90	0.037	0.993	2.28

The charge transfer mechanism accountable for the photocatalytic activity of the g-C_3N_4/ZnO-W/Co_x heterojunction can be well explained in terms of the configuration of the valance band (VB) and conduction band (CB) positions in g-C_3N_4 and ZnO using visible light irradiation. The band alignment of carbon nitride and ZnO is verified by determining potential energy level calculations using Equations (4) and (5):

$$E_{CB} = X - Ee - 0.5Eg \quad (4)$$

$$E_{VB} = E_{CB} + Eg \quad (5)$$

where E_{CB} and E_{VB} are the conduction band and valance band edge potentials, respectively, X corresponds to the electronegativity of the semiconductor and Ee represents the energy of free electrons in the hydrogen scale [65]. The X = 5.79 and 4.64 eV for ZnO and carbon nitride, whereas the band gaps of ZnO and g-C_3N_4 are 3.37 and 2.70 [66] respectively. The calculated E_{CB} and E_{VB} values for ZnO are −0.395 and 2.975 respectively, whereas for g-C_3N_4, they are −1.21 and 1.49 respectively [67]. When the g-C_3N_4/ZnO-W/M composite was irradiated with visible light, the electrons shifted from the valence band (VB) of g-C_3N_4 to its conduction band (CB). These excited electrons floated towards the CB of ZnO because the CB edge potential of g-C_3N_4 −1.21 eV is more negative than that of ZnO −0.395 eV. The doped metal acts as an electron accepter resulting in a Z-scheme heterojunction, as presented in Figure 8, and it trapped more electrons towards itself, resulting in diminished recombination of charged species in the system and it being responsible for the amplified photocatalytic activity of the synthesized catalyst.

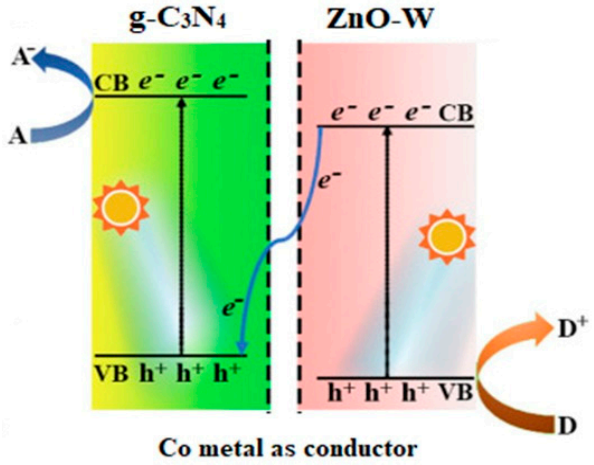

Figure 8. Hybrid Z-scheme heterojunction in dopant (Co)'s presence.

2.7. Active Species Analysis and Reusability Test

To probe the role of the key scavenger for MB degradation by the as-synthesized hybrid composite g-C_3N_4/ZnO-W/$Co_{(0.010)}$ under sunlight irradiation, ammonium oxalate (AO), isopropanol (IPA) and benzoquinone (BQ) scavengers were used as trapping agents to remove holes (h^+), hydroxyl radicals ($^{\cdot}OH$) and superoxide radicals ($^{\cdot}O^{2-}$), respectively [51]. The degradation efficiency of MB was suppressed by 92 to 31.28 % when BQ was added to the dye solution. In the same way, the addition of (AO) deteriorated the degradation efficacy from 95 to 75 %. In addition, the dye degradation efficiency was reduced to 61% upon the introduction of (IPA). Thus, it is obvious from the experimental results that the holes act as dominant oxidative species and superoxide radicals correspond to the minor oxidative species in the photodegradation mechanism, whereas the hydroxyl radicals act as a second oxidative species during the photodegradation of methylene blue. The MB dye degradation performance on g-C_3N_4/ZnO-W/$Co_{(0.010)}$ compared with other catalysts is shown in Table 3.

Table 3. Comparison of the MB dye degradation results with the published literature.

Catalyst	Catalyst (g/L)	Irradiation Time	Irradiation Source	% Degradation	Reference
$Ca_{0.5}Pb_{0.5-x}Yb_xZn_yFe_{12-y}O_{19}$	0.5 g/L	90 min	Visible light	96.1%	[68]
ZnO/PMOS	10 mg/30 mL	60 min	Visible light	48%	[69]
Urea and $[Zn(hmp\text{-}H)_2(H_2O)(\mu\text{-}Cl)Zn(\mu\text{-}Cl)(Cl)_3]$	0.02 g/L	150 min	Visible light	84%	[70]
g-C_3N_4-PANI	100 mg/L	160 min	Visible light	92%	[71]
Ag/g-C_3N_4 hybrid catalyst	1 g/L	300 min	300 W Xe lamp	58%	[72]
g-C_3N_4/TiO_2 films	NM	180 min	50 W Halogen Lamp	68%	[54]
ZnO/rGO	1.5 g/L	250 min	Hg lamp, 500 W	88%	[73]
g-C_3N_4/ZnO-W/$Co_{(0.010)}$	0.05 mg/L	90 min	Visible light	90%	Present work

2.8. Reusability Test

The stability of the fabricated hybrid composite g-C_3N_4/ZnO-W/Co_x was analyzed by conducting recyclability and reusability experiments for five cyclic runs, as shown in Figure 9d. The photocatalyst used was re-collected via centrifugation at the end of every experimental run, rinsed thrice with distilled water and dried using an oven at 70 °C. After each catalytic cycle, the catalyst was weighed and examined for its efficacy in degradation. The catalyst was reused for the next cycle by keeping the other conditions identical. The photocatalytic degradation efficiency was found to be almost the same for all reactions, and a minor abatement in activity with every cyclic run was attributed to the loss in the amount of photocatalyst during the process of recollection. This demonstrates that the reported hybrid heterojunctions exhibit high mechanical stability and reusability.

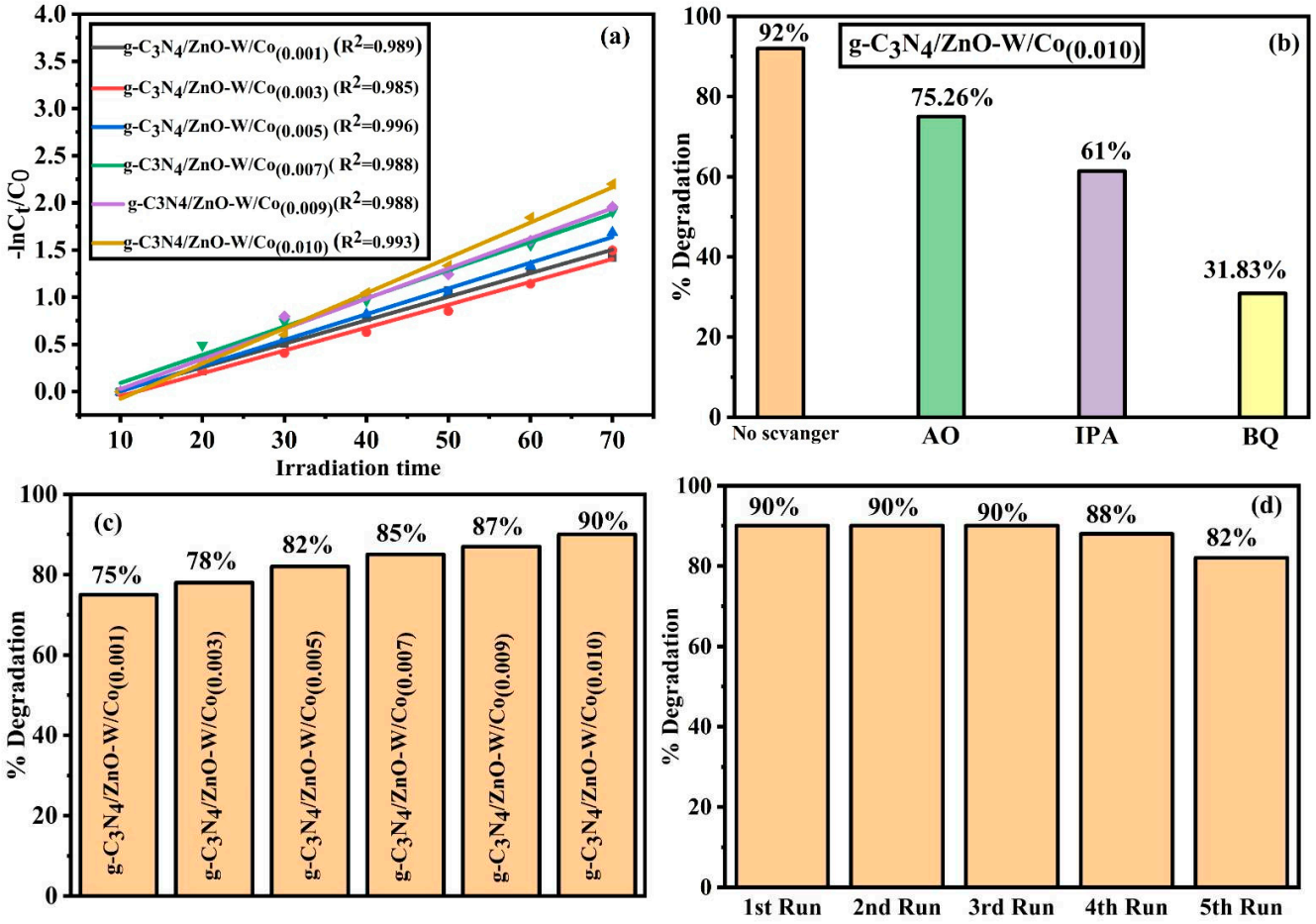

Figure 9. (**a**) Linear fit. Model kinetics plots for the MB dye. (**b**) Influence of radical scavengers on the photodegradation of MB. (**c**) % degradation of the g-C_3N_4/ZnO-W/Co_x hybrid composite. (**d**) Reusability experiment of the hybrid composite g-C_3N_4/ZnO-W/Co_x for the photocatalytic degradation of MB dye.

3. Materials and Methods

3.1. Materials

Urea (NH_2CONH_2) 99%, cobalt acetate tetrahydrate ($Co(CH_3COO)_2.4H_2O$) 99%, sodium hydroxide (NaOH) 98%, sodium tungstate (Na_2WO_4) 97.0%, zinc sulphate heptahydrate ($ZnSO_4.7H_2O$) 99%, hydrochloric acid (HCl) 37%, ethanol (analytical grade), methylene blue and distilled water. All materials are from a commercial source (Sigma Aldrich, St. Louis, MO, USA) and were used without extra purification.

3.2. Synthesis of g-C_3N_4

The g-C_3N_4 was synthesized by temperature-controlled single-step polymerization of nitrogen-rich compound urea as a precursor. Approximately 10 g of urea was placed into a crucible. Then, the sample was heated using a temperature-controlled programmed up to 550 °C for 5 h. The yellow-coloured g-C_3N_4 was collected in solid form and ground to form fine powder in a mortar and then used for further modification [44].

3.3. Synthesis of ZnO (NPs)

ZnO (NPs) was prepared by dissolving 5 mmol of zinc sulphate heptahydrate (1.485 g) in 50 ml of deionized water. Then, an equimolar amount of NaOH (0.2 g dissolved in water) was added dropwise and the pH was maintained at 9. The mixture was then stirred for 12 h. Yellowish precipitates of zinc oxide were obtained by filtration and then dried at 100 °C in a furnace for 2 h. The obtained product was ground to form a fine powder and calcined at 500 °C for 5 h. As a result, zinc oxide nanoparticles were obtained [44].

3.4. Synthesis of the g-C_3N_4/ZnO-W Composite

The g-C_3N_4/ZnO-W (W = tungsten) was synthesized by dissolving 1 g of previously prepared g-C_3N_4 in 40 mL of deionized water. Then, 0.05 g of ZnO NPs and 0.01 g of sodium tungstate were dispersed in 30 mL of deionized water, and the solution was ultrasonicated for 30 min. Both solutions were mixed together and transferred to a round bottom flask. Approximately 10 mL of 0.1 M NaOH was added dropwise to the mixture solution and stirred vigorously for about 8 h. The final product g-C_3N_4/ZnO-W formed was washed with deionized water and ethanol several times and dried at 60 °C for about 48 h [44].

3.5. Synthesis of the g-C_3N_4/ZnO-W/Co_x Nanocomposites

For the preparation of g-C_3N_4/ZnO-W/Co_x, 1 g of the synthesized g-C_3N_4/ZnO-W composite was dissolved in 50 mL of deionized water. After that, Co $(CH_3COO)_2.4H_2O$ with different concentrations (x = 0.001, 0.003, 0.005, 0.007, 0.009 and 0.01 M) was added and sonicated for 30 min. The pH of the solution was maintained at 9 by dropwise addition of NaOH. Then, the whole solution was shifted to a round bottom flask and stirred for 8 h. After that filtration, the product obtained was subsequently dried at 100 °C for 12 h. The schematic representation of the synthesis of the g-C_3N_4/ZnO-W/Co_x hybrid composites is shown in Figure 10 [44].

3.6. Photocatalytic Activity

The photocatalytic activity of the synthesized nanocomposites for methylene blue was examined by using a UV–visible spectrophotometer (Shimadzu UV-1240, Shimadzu Europe). The photocatalytic experiment was carried out on consecutive sunny days between 10 a.m. to 1 p.m. in the month of March (Pakistan). The flux density of the sunlight was determined using a digital flux meter with 20 min time intervals. The calculated flux density was 64,520 ± 100 This result confirms that sunlight intensity remains constant during the experiments. Firstly, a 10 ppm solution of MB dye was prepared in distilled water where 0.05 mg of the synthesized composite was dispersed. The solution was allowed to stir continuously for 1 h under dark conditions to attain adsorption–desorption equilibrium between the catalyst and dye. After this solution was continuously stirred for 90 min under sunlight illumination and after every 15 min interval, the sequential samples were

investigated to record the UV visible absorption spectrum at λ_{max} = 665 nm to estimate the degradation efficiency of the catalyst [74,75]. The percentage degradation was calculated using the mathematical expression (6).

$$\text{Degradation efficiency } (\eta) = C_0 - C_t/C_0 \times 100 \quad (6)$$

where C_0 is the initial concentration of the dye solution and C_t is the concentration of the dye solution measured at different time intervals during the photocatalytic reaction.

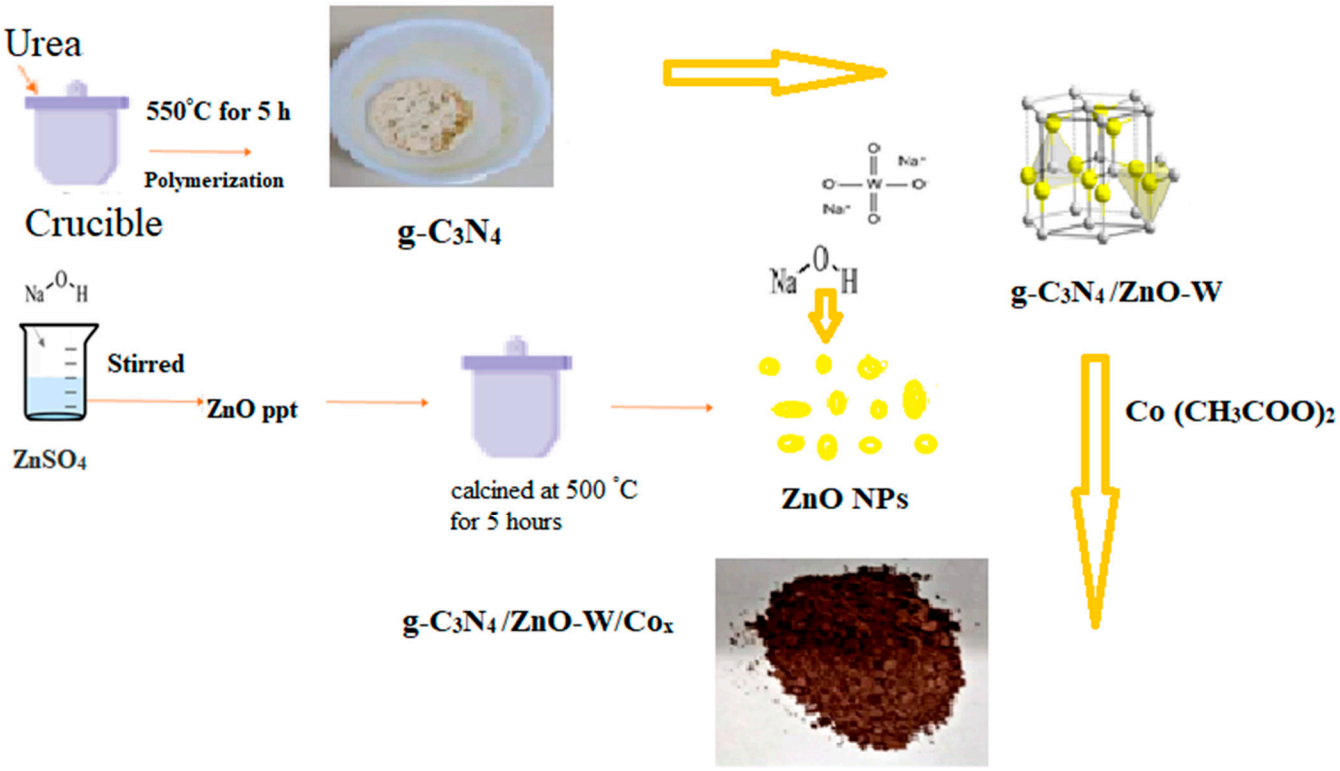

Figure 10. Schematic representation of the synthesis of the g-C_3N_4/ZnO-W/Co_x hybrid heterojunction nanocomposites.

3.7. Characterisation

Structural parameters of the synthesized composites such as the average crystallite size (D), lattice parameters (a and c) and unit cell volume (Vcell) were investigated by a JEOL X-ray diffraction meter fortified with CuKα radiations (wavelength = 1.5418 Å) (Tokyo, Japan). An Alpha-Bruker Fourier transform infrared spectrophotometer (FTIR) (Mannheim, Germany) was used for structural elucidations of the synthesized hybrid nanocomposites. Meanwhile, energy-dispersive X-ray spectroscopy (EDX) spectra of the samples were obtained using INCA 100 (Oxford, UK, JEM-2100). The morphological analysis of the synthesized composites was affirmed by a scanning electron microscope (JEOL, Japan JSM5910). On the other hand, a UV–visible spectrophotometer (Cecil CE 7400, Waltham, MA, USA) was used to record the absorbance of the dye solutions.

4. Conclusions

This research aimed to investigate the effect of cobalt doping on the electronic, optical, morphological, physical and photocatalytic properties of g-C_3N_4 and ZnO. The series of g-C_3N_4 /ZnO-W materials doped with various concentrations of cobalt were synthesized via the coprecipitation method. The XRD and FTIR analyses indicated the formation of hybrid heterojunctions g-C_3N_4/ZnO-W/Co_x composites. The analyses revealed that pristine ZnO exhibits less activity as compared to the W-doped material because the W-ion generates

an intermediate energy level between the valance band and the conduction band, causing the deception of photo-excited electrons from the conduction band level. This deception of electrons in the intermediate level deferred the recombination of the electron–hole pair resulting in enhanced photocatalytic activity. Another advantage associated with tungsten as a dopant is its ionic state, i.e., W^{+6}. When Zn^{+2} is replaced by W^{+6}, the number of charge carriers increases in the ZnO system of the semiconductor material, and an improved degradation efficacy can be attained. The structural and optical analyses were used to study the doping effect of metal which revealed greatly improved charge carrier separation and suppressed their recombination. The effective consequences were in favor of the remarkably enhanced light absorption, photodegradation and reusability efficiencies of the synthesized materials for organic dye.

Author Contributions: M.M. and A.A. performed the experiments and prepared the original draft. M.A.N., M.K.T. and S.S.A.S. performed the data curation and editing and revision of the draft. M.A.W. helped with the manuscript preparation and data interpretation. S.M.I. and A.A.T. performed the spectroscopic analysis. A.u.R. initiated the idea and supervised the project. All authors have read and agreed to the published version of the manuscript.

Funding: Researchers Supporting Project number (RSP2023R100).

Data Availability Statement: All relevant data may be provided upon request.

Acknowledgments: This work was supported by Researchers Supporting Project number (RSP2023R100), King Saud University, Riyadh, Saudi Arabia. The authors also gratefully acknowledge the Ph.D. analytical laboratory, Institute of Chemistry, Islamia University of Bahawalpur, for providing the experimental and analytical facilities.

Conflicts of Interest: The authors declare no conflict of interests or personal relationships that could have appeared to have influenced the work reported in this paper.

References

1. Das, R. Application photocatalysis for treatment of industrial waste water—A short review. *Open Access Libr. J.* **2014**, *1*, 1–17. [CrossRef]
2. Yuan, L.; Geng, Z.; Zhang, S.; Xu, J.; Guo, F.; Kumar Kundu, B.; Han, C. Efficient all-in-one removal of total chromium over nonconjugated polymer-inorganic ZnIn2S4 semiconductor hybrid. *J. Colloid Interface Sci.* **2022**, *628*, 100–108. [CrossRef] [PubMed]
3. Md Rosli, N.I.; Lam, S.-M.; Sin, J.-C.; Satoshi, I.; Mohamed, A.R. Photocatalytic Performance of ZnO/g-C 3 N 4 for Removal of Phenol under Simulated Sunlight Irradiation. *J. Environ. Eng.* **2018**, *144*, 04017091. [CrossRef]
4. Zhao, Z.; Sun, Y.; Dong, F. Graphitic carbon nitride based nanocomposites: A review. *Nanoscale* **2015**, *7*, 15–37. [CrossRef]
5. Ong, W.-J.; Tan, L.-L.; Chai, S.-P.; Yong, S.-T. Graphene oxide as a structure-directing agent for the two-dimensional interface engineering of sandwich-like graphene–gC_3N_4 hybrid nanostructures with enhanced visible-light photoreduction of CO_2 to methane. *Chem. Commun.* **2015**, *51*, 858–861. [CrossRef]
6. Yang, C.; Xue, Z.; Qin, J.; Sawangphruk, M.; Rajendran, S.; Zhang, X.; Liu, R. Visible light-driven photocatalytic H_2 generation and mechanism insights into $Bi_2O_2CO_3$/G-C_3N_4 Z-scheme photocatalyst. *J. Phys. Chem. C* **2019**, *123*, 4795–4804. [CrossRef]
7. Farooq, N.; Luque, R.; Hessien, M.M.; Qureshi, A.M.; Sahiba, F.; Nazir, M.A.; ur Rehman, A. A Comparative Study of Cerium- and Ytterbium-Based GO/g-C_3N_4/Fe_2O_3 Composites for Electrochemical and Photocatalytic Applications. *Appl. Sci.* **2021**, *11*, 9000. [CrossRef]
8. Qin, J.; Zhang, M.; Rajendran, S.; Zhang, X.; Liu, R. Two-dimensional porous sheet-like carbon-doped ZnO/g-C_3N_4 nanocomposite with high visible-light photocatalytic performance. *Mater. Lett.* **2017**, *189*, 156–159. [CrossRef]
9. Kumar, O.P.; Shahzad, K.; Nazir, M.A.; Farooq, N.; Malik, M.; Ahmad Shah, S.S.; Rehman, A.u. Photo-Fenton activated C_3N_{4x}/AgO_y@$Co_{1-x}Bi_{0.1-y}O_7$ dual s-scheme heterojunction towards degradation of organic pollutants. *Opt. Mater.* **2022**, *126*, 112199. [CrossRef]
10. Yang, C.; Qin, J.; Rajendran, S.; Zhang, X.; Liu, R. WS2 and C-TiO_2 nanorods acting as effective charge separators on g-C_3N_4 to boost visible-light activated hydrogen production from seawater. *ChemSusChem* **2018**, *11*, 4077–4085. [CrossRef] [PubMed]
11. Tong, T.; Zhu, B.; Jiang, C.; Cheng, B.; Yu, J. Mechanistic insight into the enhanced photocatalytic activity of single-atom Pt, Pd or Au-embedded g-C_3N_4. *Appl. Surf. Sci.* **2018**, *433*, 1175–1183. [CrossRef]
12. Liu, S.; Li, D.; Sun, H.; Ang, H.M.; Tadé, M.O.; Wang, S. Oxygen functional groups in graphitic carbon nitride for enhanced photocatalysis. *J. Colloid Interface Sci.* **2016**, *468*, 176–182. [CrossRef]
13. Kheirabadi, M.; Samadi, M.; Asadian, E.; Zhou, Y.; Dong, C.; Zhang, J.; Moshfegh, A.Z. Well-designed Ag/ZnO/3D graphene structure for dye removal: Adsorption, photocatalysis and physical separation capabilities. *J. Colloid Interface Sci.* **2019**, *537*, 66–78. [CrossRef]

14. Fu, X.; Hu, X.; Yan, Z.; Lei, K.; Li, F.; Cheng, F.; Chen, J. Template-free synthesis of porous graphitic carbon nitride/carbon composite spheres for electrocatalytic oxygen reduction reaction. *Chem. Commun.* **2016**, *52*, 1725–1728. [CrossRef] [PubMed]
15. Wang, X.; Maeda, K.; Thomas, A.; Takanabe, K.; Xin, G.; Carlsson, J.M.; Domen, K.; Antonietti, M. A metal-free polymeric photocatalyst for hydrogen production from water under visible light. *Nat. Mater.* **2009**, *8*, 76–80. [CrossRef]
16. Wen, J.; Xie, J.; Chen, X.; Li, X. A review on g-C3N4-based photocatalysts. *Appl. Surf. Sci.* **2017**, *391*, 72–123. [CrossRef]
17. Su, F.; Mathew, S.C.; Lipner, G.; Fu, X.; Antonietti, M.; Blechert, S.; Wang, X. mpg-C_3N_4-catalyzed selective oxidation of alcohols using O_2 and visible light. *J. Am. Chem. Soc.* **2010**, *132*, 16299–16301. [CrossRef]
18. Zhang, Y.; Liu, J.; Wu, G.; Chen, W. Porous graphitic carbon nitride synthesized via direct polymerization of urea for efficient sunlight-driven photocatalytic hydrogen production. *Nanoscale* **2012**, *4*, 5300–5303. [CrossRef] [PubMed]
19. Zhou, X.; Shao, C.; Yang, S.; Li, X.; Guo, X.; Wang, X.; Li, X.; Liu, Y. Heterojunction of g-C_3N_4/BiOI immobilized on flexible electrospun polyacrylonitrile nanofibers: Facile preparation and enhanced visible photocatalytic activity for floating photocatalysis. *Acs Sustain. Chem. Eng.* **2018**, *6*, 2316–2323. [CrossRef]
20. Kumar, O.P.; Ahmad, M.; Nazir, M.A.; Anum, A.; Jamshaid, M.; Shah, S.S.A.; Rehman, A. Strategic combination of metal–organic frameworks and C_3N_4 for expeditious photocatalytic degradation of dye pollutants. *Environ. Sci. Pollut. Res.* **2022**, *29*, 35300–35313. [CrossRef] [PubMed]
21. Wan, W.; Yu, S.; Dong, F.; Zhang, Q.; Zhou, Y. Efficient C_3N_4/graphene oxide macroscopic aerogel visible-light photocatalyst. *J. Mater. Chem. A* **2016**, *4*, 7823–7829. [CrossRef]
22. Zhang, R.; Ma, M.; Zhang, Q.; Dong, F.; Zhou, Y. Multifunctional g-C_3N_4/graphene oxide wrapped sponge monoliths as highly efficient adsorbent and photocatalyst. *Appl. Catal. B Environ.* **2018**, *235*, 17–25. [CrossRef]
23. Li, R.; Cai, M.; Xie, Z.; Zhang, Q.; Zeng, Y.; Liu, H.; Liu, G.; Lv, W. Construction of heterostructured $CuFe_2O_4$/g-C_3N_4 nanocomposite as an efficient visible light photocatalyst with peroxydisulfate for the organic oxidation. *Appl. Catal. B Environ.* **2019**, *244*, 974–982. [CrossRef]
24. Liang, M.; Borjigin, T.; Zhang, Y.; Liu, B.; Liu, H.; Guo, H. Controlled assemble of hollow heterostructured g-C_3N_4@ CeO_2 with rich oxygen vacancies for enhanced photocatalytic CO_2 reduction. *Appl. Catal. B Environ.* **2019**, *243*, 566–575. [CrossRef]
25. Xiao, T.; Tang, Z.; Yang, Y.; Tang, L.; Zhou, Y.; Zou, L. In situ construction of hierarchical WO3/g-C3N4 composite hollow microspheres as a Z-scheme photocatalyst for the degradation of antibiotics. . *Appl. Catal. B Environ.* **2018**, *220*, 417–428. [CrossRef]
26. Di, T.; Zhu, B.; Cheng, B.; Yu, J.; Xu, J. A direct Z-scheme g-C_3N_4/SnS_2 photocatalyst with superior visible-light CO_2 reduction performance. *J. Catal.* **2017**, *352*, 532–541. [CrossRef]
27. Huang, Z.; Zeng, X.; Li, K.; Gao, S.; Wang, Q.; Lu, J. Z-scheme $NiTiO_3$/g-C_3N_4 heterojunctions with enhanced photoelectrochemical and photocatalytic performances under visible LED light irradiation. *ACS Appl. Mater. Interfaces* **2017**, *9*, 41120–41125. [CrossRef] [PubMed]
28. Kundu, B.K.; Han, G.; Sun, Y. Derivatized benzothiazoles as two-photon-absorbing organic photosensitizers active under near infrared light irradiation. *J. Am. Chem. Soc.* **2023**, *145*, 3535–3542. [CrossRef]
29. Wu, Z.; Kundu, B.K.; Kang, W.; Mao, L.; Zhang, S.; Yuan, L.; Guo, F.; Han, C. Self-adaptive bulk/surface engineering of BixOyBrz towards enhanced photocatalysis: Current status and future challenges. *J. Energy Chem.* 2023, *in press*.
30. Gomez, J.L.; Tigli, O. Zinc oxide nanostructures: From growth to application. *J. Mater. Sci.* **2013**, *48*, 612–624. [CrossRef]
31. Sakthivel, S.; Neppolian, B.; Shankar, M.; Arabindoo, B.; Palanichamy, M.; Murugesan, V. Solar photocatalytic degradation of azo dye: Comparison of photocatalytic efficiency of ZnO and TiO_2. *Sol. Energy Mater. Sol. Cells* **2003**, *77*, 65–82. [CrossRef]
32. Li, Y.; Xie, W.; Hu, X.; Shen, G.; Zhou, X.; Xiang, Y.; Zhao, X.; Fang, P. Comparison of dye photodegradation and its coupling with light-to-electricity conversion over TiO_2 and ZnO. *Langmuir* **2010**, *26*, 591–597. [CrossRef] [PubMed]
33. Dindar, B.; Içli, S. Unusual photoreactivity of zinc oxide irradiated by concentrated sunlight. *J. Photochem. Photobiol. A Chem.* **2001**, *140*, 263–268. [CrossRef]
34. Gouvea, C.A.; Wypych, F.; Moraes, S.G.; Duran, N.; Nagata, N.; Peralta-Zamora, P. Semiconductor-assisted photocatalytic degradation of reactive dyes in aqueous solution. *Chemosphere* **2000**, *40*, 433–440. [CrossRef]
35. Laouedj, E.; Ahmed, B. ZnOAssisted Photocatalytic Degradation of Congo Red and Benzopurpurine 4B in Aqueous Solution. *J. Chem. Eng. Process Technol.* **2011**, *2*, 1–9.
36. Zhu, L.; Liu, Z.; Xia, P.; Li, H.; Xie, Y. Synthesis of hierarchical ZnO&Graphene composites with enhanced photocatalytic activity. *Ceram. Int.* **2018**, *44*, 849–856.
37. Qi, K.; Cheng, B.; Yu, J.; Ho, W. Review on the improvement of the photocatalytic and antibacterial activities of ZnO. *J. Alloys Compd.* **2017**, *727*, 792–820. [CrossRef]
38. Kumar, S.; Dhiman, A.; Sudhagar, P.; Krishnan, V. ZnO-graphene quantum dots heterojunctions for natural sunlight-driven photocatalytic environmental remediation. *Appl. Surf. Sci.* **2018**, *447*, 802–815. [CrossRef]
39. Luu Thi, L.A.; Neto, M.M.; Van, T.P.; Nguyen Ngoc, T.; Nguyen Thi, T.M.; Nguyen, X.S.; Nguyen, C.T. In Situ g-C_3N_4@ Zno Nanocomposite: One-Pot Hydrothermal Synthesis and Photocatalytic Performance under Visible Light Irradiation. *Adv. Mater. Sci. Eng.* **2021**, *2021*, 6651633. [CrossRef]
40. Iqbal, J.; Liu, X.; Zhu, H.; Wu, Z.; Zhang, Y.; Yu, D.; Yu, R. Raman and highly ultraviolet red-shifted near band-edge properties of LaCe-co-doped ZnO nanoparticles. *Acta Mater.* **2009**, *57*, 4790–4796. [CrossRef]

41. Ngom, B.; Mpahane, T.; Manyala, N.; Nemraoui, O.; Buttner, U.; Kana, J.; Fasasi, A.; Maaza, M.; Beye, A. Structural and optical properties of nano-structured tungsten-doped ZnO thin films grown by pulsed laser deposition. *Appl. Surf. Sci.* **2009**, *255*, 4153–4158. [CrossRef]
42. Ahmad, K.; Nazir, M.A.; Qureshi, A.K.; Hussain, E.; Najam, T.; Javed, M.S.; Shah, S.S.A.; Tufail, M.K.; Hussain, S.; Khan, N.A.; et al. Engineering of Zirconium based metal-organic frameworks (Zr-MOFs) as efficient adsorbents. *Mater. Sci. Eng. B* **2020**, *262*, 114766. [CrossRef]
43. Shahzad, K.; Nazir, M.A.; Jamshaid, M.; Kumar, O.P.; Najam, T.; Shah, S.S.A.; Rehman, A. Synthesis of nanoadsorbent entailed mesoporous organosilica for decontamination of methylene blue and methyl orange from water. *Int. J. Environ. Anal. Chem.* **2021**, 1–14. [CrossRef]
44. Malik, M.; Len, T.; Luque, R.; Osman, S.M.; Paone, E.; Khan, M.I.; Wattoo, M.A.; Jamshaid, M.; Anum, A.; ur Rehman, A. Investigation on synthesis of hybrid g-C_3N_4/ZnO–W/M nanocomposites integrated heterojunction II as efficient photocatalyst for environmental applications. *Environ. Res.* **2023**, *217*, 114621. [CrossRef]
45. Paul, D.R.; Sharma, R.; Panchal, P.; Nehra, S.; Gupta, A.; Sharma, A. Synthesis, characterization and application of silver doped graphitic carbon nitride as photocatalyst towards visible light photocatalytic hydrogen evolution. *Int. J. Hydrogen Energy* **2020**, *45*, 23937–23946. [CrossRef]
46. Tian, H.; Fan, H.; Ma, J.; Liu, Z.; Ma, L.; Lei, S.; Fang, J.; Long, C. Pt-decorated zinc oxide nanorod arrays with graphitic carbon nitride nanosheets for highly efficient dual-functional gas sensing. *J. Hazard. Mater.* **2018**, *341*, 102–111. [CrossRef] [PubMed]
47. Wang, X.; Hong, M.; Zhang, F.; Zhuang, Z.; Yu, Y. Recyclable nanoscale zero valent iron doped g-C_3N_4/MoS_2 for efficient photocatalysis of RhB and Cr (VI) driven by visible light. *ACS Sustain. Chem. Eng.* **2016**, *4*, 4055–4063. [CrossRef]
48. Tahir, N.; Zahid, M.; Bhatti, I.A.; Jamil, Y. Fabrication of Visible Light Active Mn-Doped Bi_2WO_6-GO/MoS_2 Heterostructure for Enhanced Photocatalytic Degradation of Methylene Blue. *Environ. Sci. Pollut. Res.* **2021**, *29*, 6552–6567. [CrossRef]
49. Nyquist, R.A.; Kagel, R.O. *Handbook of Infrared and Raman Spectra of Inorganic Compounds and Organic Salts: Infrared Spectra of Inorganic Compounds*; Academic Press: Cambridge, MA, USA, 2012; Volume 4.
50. Al-Hajry, A.; Umar, A.; Hahn, Y.; Kim, D. Growth, properties and dye-sensitized solar cells–applications of ZnO nanorods grown by low-temperature solution process. *Superlattices Microstruct.* **2009**, *45*, 529–534. [CrossRef]
51. Sher, M.; Javed, M.; Shahid, S.; Iqbal, S.; Qamar, M.A.; Bahadur, A.; Qayyum, M.A. The controlled synthesis of gC_3N_4/Cd-doped ZnO nanocomposites as potential photocatalysts for the disinfection and degradation of organic pollutants under visible light irradiation. *RSC Adv.* **2021**, *11*, 2025–2039. [CrossRef]
52. Le, S.; Jiang, T.; Li, Y.; Zhao, Q.; Li, Y.; Fang, W.; Gong, M. Highly efficient visible-light-driven mesoporous graphitic carbon nitride/ZnO nanocomposite photocatalysts. *Appl. Catal. B Environ.* **2017**, *200*, 601–610. [CrossRef]
53. Kumaresan, S.; Vallalperuman, K.; Sathishkumar, S. A Novel one-step synthesis of Ag-doped ZnO nanoparticles for high performance photo-catalytic applications. *J. Mater. Sci. Mater. Electron.* **2017**, *28*, 5872–5879. [CrossRef]
54. Boonprakob, N.; Wetchakun, N.; Phanichphant, S.; Waxler, D.; Sherrell, P.; Nattestad, A.; Chen, J.; Inceesungvorn, B. Enhanced visible-light photocatalytic activity of g-C_3N_4/TiO_2 films. *J. Colloid Interface Sci.* **2014**, *417*, 402–409. [CrossRef]
55. Ravichandran, K.; Seelan, K.S.; Ibrahim, M.M.; Kavitha, P. Improved solar light responsive photocatalytic activity of ZnO: W films: Effect of W loading level. *Mater. Today Proc.* **2020**, *48*, 216–228. [CrossRef]
56. Vafaee, M.; Olya, M.; Drean, J.-Y.; Hekmati, A. Synthesize, characterization and application of ZnO/W/Ag as a new nanophotocatalyst for dye removal of textile wastewater; kinetic and economic studies. *J. Taiwan Inst. Chem. Eng.* **2017**, *80*, 379–390. [CrossRef]
57. Alosaimi, E.H.; Azeem, N.; Tahir, N.; Jilani, A.; Zahid, M.; Alharthi, S.; Iqbal, J.; Yaseen, M.; Ahmad Rehan, Z.; Shahid, I. Investigation of Fe-Doped Graphitic Carbon Nitride-Silver Tungstate as a Hybrid Visible Light Active Photocatalyst. *J. Chem.* **2021**, *2021*, 1–18.
58. Wojtyła, S.; Śpiewak, K.; Baran, T. Doped graphitic carbon nitride: Insights from spectroscopy and electrochemistry. *J. Inorg. Organomet. Polym. Mater.* **2020**, *30*, 3418–3428. [CrossRef]
59. Hezam, A.; Namratha, K.; Ponnamma, D.; Drmosh, Q.; Saeed, A.M.N.; Cheng, C.; Byrappa, K. Direct Z-scheme Cs_2O–Bi_2O_3–ZnO heterostructures as efficient sunlight-driven photocatalysts. *ACS Omega* **2018**, *3*, 12260–12269. [CrossRef]
60. Rahman, M.U.; Qazi, U.Y.; Hussain, T.; Nadeem, N.; Zahid, M.; Bhatti, H.N.; Shahid, I. Solar driven photocatalytic degradation potential of novel graphitic carbon nitride based nano zero-valent iron doped bismuth ferrite hybrid composite. *Opt. Mater.* **2021**, *120*, 111408. [CrossRef]
61. Neena, D.; Humayun, M.; Zuo, W.; Liu, C.; Gao, W.; Fu, D.J. Hierarchical hetero-architectures of in-situ g-C_3N_4-coupled Fe-doped ZnO micro-flowers with enhanced visible-light photocatalytic activities. *Appl. Surf. Sci.* **2020**, *506*, 145017. [CrossRef]
62. Praus, P. On electronegativity of graphitic carbon nitride. *Carbon* **2021**, *172*, 729–732. [CrossRef]
63. Wang, Y.; Cheng, J.; Yu, S.; Alcocer, E.J.; Shahid, M.; Wang, Z.; Pan, W. Synergistic effect of N-decorated and Mn^{2+} doped ZnO nanofibers with enhanced photocatalytic activity. *Sci. Rep.* **2016**, *6*, 32711. [CrossRef] [PubMed]
64. Mohite, S.; Rajpure, K. Oxidative degradation of salicylic acid by sprayed WO_3 photocatalyst. *Mater. Sci. Eng. B* **2015**, *200*, 78–83. [CrossRef]
65. Munawar, T.; Yasmeen, S.; Hussain, F.; Mahmood, K.; Hussain, A.; Asghar, M.; Iqbal, F. Synthesis of novel heterostructured ZnO-CdO-CuO nanocomposite: Characterization and enhanced sunlight driven photocatalytic activity. *Mater. Chem. Phys.* **2020**, *249*, 122983. [CrossRef]

66. Chen, S.; Hu, Y.; Meng, S.; Fu, X. Study on the separation mechanisms of photogenerated electrons and holes for composite photocatalysts g-C_3N_4-WO_3. *Appl. Catal. B Environ.* **2014**, *150*, 564–573. [CrossRef]
67. Fageria, P.; Nazir, R.; Gangopadhyay, S.; Barshilia, H.C.; Pande, S. Graphitic-carbon nitride support for the synthesis of shape-dependent ZnO and their application in visible light photocatalysts. *RSC Adv.* **2015**, *5*, 80397–80409. [CrossRef]
68. Jamshaid, M.; Nazir, M.A.; Najam, T.; Shah, S.S.A.; Khan, H.M.; Rehman, A.u. Facile synthesis of Yb^{3+}-Zn^{2+} substituted M type hexaferrites: Structural, electric and photocatalytic properties under visible light for methylene blue removal. *Chem. Phys. Lett.* **2022**, *805*, 139939. [CrossRef]
69. Shahzad, K.; Najam, T.; Bashir, M.S.; Nazir, M.A.; ur Rehman, A.; Bashir, M.A.; Shah, S.S.A. Fabrication of Periodic Mesoporous Organo Silicate (PMOS) composites of Ag and ZnO: Photo-catalytic degradation of methylene blue and methyl orange. *Inorg. Chem. Commun.* **2021**, *123*, 108357. [CrossRef]
70. Mohammad, A.; Ahmad, K.; Qureshi, A.; Tauqeer, M.; Mobin, S.M. Zinc oxide-graphitic carbon nitride nanohybrid as an efficient electrochemical sensor and photocatalyst. *Sens. Actuators B Chem.* **2018**, *277*, 467–476. [CrossRef]
71. Ge, L.; Han, C.; Liu, J. In situ synthesis and enhanced visible light photocatalytic activities of novel PANI-g-C_3N_4 composite photocatalysts. *J. Mater. Chem.* **2012**, *22*, 11843–11850. [CrossRef]
72. Meng, Y.; Shen, J.; Chen, D.; Xin, G. Photodegradation performance of methylene blue aqueous solution on Ag/g-C_3N_4 catalyst. *Rare Met.* **2011**, *30*, 276–279. [CrossRef]
73. Lv, T.; Pan, L.; Liu, X.; Lu, T.; Zhu, G.; Sun, Z. Enhanced photocatalytic degradation of methylene blue by ZnO-reduced graphene oxide composite synthesized via microwave-assisted reaction. *J. Alloys Compd.* **2011**, *509*, 10086–10091. [CrossRef]
74. Nazir, M.A.; Khan, N.A.; Cheng, C.; Shah, S.S.A.; Najam, T.; Arshad, M.; Sharif, A.; Akhtar, S.; ur RehmanRehman, A. Surface induced growth of ZIF-67 at Co-layered double hydroxide: Removal of methylene blue and methyl orange from water. *Appl. Clay Sci.* **2020**, *190*, 105564. [CrossRef]
75. Jamshaid, M.; ur Rehman, A.; Kumar, O.P.; Iqbal, S.; Nazir, M.A.; Anum, A.; Khan, H.M. Design of dielectric and photocatalytic properties of Dy–Ni substituted $Ca_{0.5}Pb_{0.5-x}Fe_{12-y}O_{19}$ M-type hexaferrites. *J. Mater. Sci. Mater. Electron.* **2021**, *32*, 16255–16268. [CrossRef]